Measuring the state and temporal evolution of glaciers using SAR-derived 3D time series of glacier surface flow

Sergey Samsonov[1], Kristy Tiampo[2], and Ryan Cassotto[2]

[1]Canada Centre for Mapping and Earth Observation, Natural Resources Canada, 560 Rochester Street, Ottawa, ON K1S5K2 Canada
[2]Earth Science & Observation Center, Cooperative Institute for Research in Environmental Sciences, University of Colorado, Boulder, CO 80309 USA

Correspondence: Sergey Samsonov (sergey.samsonov@canada.ca)

Abstract. The direction and intensity of glacier surface flow adjust in response to a warming climate, causing sea level rise, seasonal flooding and droughts, changing landscapes and habitats. However, until recently no single technique could consistently measure the evolution of surface flow for an entire glaciated region in three-dimensions with high temporal and spatial resolutions. We have developed such a technique and use it to map, in unprecedented detail, the temporal evolution of five glaciers in southeastern Alaska (Agassiz, Seward, Malaspina, Klutlan and Walsh) during 2016-2020. We observe seasonal and interannual variations and the maximum horizontal and vertical flow velocity in excess of 1000 and 200 m/year, respectfully. We also observe culminating phases of surging at Klutlan and Walsh glaciers and confirm that Agassiz, Seward and Malaspina glaciers continue to adjust to a warming climate. On a broader scale, this technique can be used for reconstructing the response of worldwide glaciers to the warming climate using nearly 30 years of archived SAR data and for near real-time monitoring of these glaciers using rapid revisit SAR data from satellites, such as Sentinel-1 (6 days revisit period) and forthcoming NISAR (12 days revisit period).

1 Introduction

Glacier dynamics, specifically the direction and intensity of glacier flow, adjust in response to the warming climate, leading to changes in seasonal flooding and droughts, landscapes and habitats, and ultimately sea-level variations. Surface flow is a key variable for determining glacier mass balance (Shepherd et al., 2020), ice thickness (Werder et al., 2020; Morlighem et al., 2011) and surface mass balance (Bisset et al., 2020). However, until recently no single technique could consistently measure the temporal evolution of surface flow for an entire glaciated region in three-dimensions (3D) and with high temporal and spatial resolutions.

Modern remote sensing techniques used for monitoring glacier flow include Synthetic Aperture Radar (SAR) (Goldstein et al., 1993; Mohr et al., 1998; Rignot, 2002; Joughin, 2002), Global Navigation Satellite System (GNSS) (van de Wal et al., 2008; Bartholomew et al., 2010), optical imagery (Berthier et al., 2005; Herman et al., 2011; Dehecq et al., 2015; Fahnestock et al., 2016), and uncrewed aerial vehicles (Immerzeel et al., 2014). Among these techniques, SAR is the only active side-looking sensor with global coverage at high temporal and spatial resolutions that can operate in any weather conditions, day or

night. SAR techniques comprise meter-scale speckle offset tracking (SPO) (Strozzi et al., 2002) and split-beam interferometry

25 (or multi-aperture interferometry, MAI) (Bechor and Zebker, 2006; Gourmelen et al., 2011), and centimeter-scale differential interferometry (DInSAR) (Massonnet and Feigl, 1995; Rosen et al., 2000). SPO applies image correlation algorithms to radar backscatter to measure displacements in the satellite range and azimuth directions using two SAR images. Since its early inception SAR has been used in glacier monitoring for estimating flow velocities, surface flux, tidal variations, grounding line behavior and subglacial lake activity (Goldstein et al., 1993; Joughin et al., 1995, 1998; Rignot, 1998; Shepherd et al., 2001;

30 Gray et al., 2005; Palmer et al., 2010; Minchew et al., 2017).

Southeast Alaska has experienced significant ice mass loss and retreat over the last 50 years (Arendt et al., 2009; Arendt, 2011). Of the 27,000 glaciers that occupy the region, the majority (99.8%) are non-tidewater (RGIConsortium, 2017). Consequently, monitoring the mass balance and ice dynamic variations of Alaska's land-terminating glaciers is paramount for the future of its landscape and resultant contributions to sea level rise (Larsen et al., 2015). Unlike the plethora of ice velocity

35 data products available for Greenland and Antarctica, regional studies of Alaskan glacier surface velocities pale in comparison. The first regional map of Alaskan glacier flow velocities was released in 2013 using ALOS PALSAR data (Burgess et al., 2013). Soon after, feature tracking of Landsat optical data began to regularly map regional surface velocities (Fahnestock et al., 2015; Gardner et al., 2018, 2019). Recent studies demonstrate the importance of characterizing the temporal evolution of glacier surface flow for understanding changes in ice dynamics in Alaska (Waechter et al., 2015; Altena et al., 2019). However,

40 all regional studies of Alaskan glacier flow have so far been limited to two dimensions; thus, ignoring an important vertical component of flow. Here, we introduce methods to generate a dense record of regional Alaskan glacier surface flow in three dimensions.

Historically, three components of glacier velocity using DInSAR and/or range offsets were computed by introducing a surface-parallel flow (SPF) constraint. This approach was used for 3D mapping of Antarctic (Rignot et al., 2011), Greenlandic

45 (Joughin et al., 1998; Mohr et al., 1998) and Himalayan (Kumar et al., 2011) glaciers and validated by independent GPS (Kumar et al., 2011) and MAI (Gourmelen et al., 2011) measurements. In our previous work, we adopted the SPF method for computing the 3D flow displacement time series of the Barnes Ice Cap using ascending and descending DInSAR data (Samsonov, 2019). However, the SPF constraint is only applicable to glaciers that are in a steady-state. Previous studies that used ascending and descending DInSAR (Gray, 2011) or SPO range and azimuth offsets (Wang et al., 2019) computed 3D glacier velocities

50 with coarse temporal resolution. Recently, Guo et al. (2020) developed a technique that utilized the Multidimensional Small Baseline Subset (MSBAS) approach (Samsonov and d'Oreye, 2012, 2017; Samsonov, 2019; Samsonov et al., 2020) to invert SPO ascending and descending range and azimuth offsets for studying Hispar Glacier in Central Karakoram. Here, we present our independently developed version of this algorithm that is conceptually similar to the technique developed by Guo et al. (2020) but is different in both implementation and choice of processing options. Specifically, it can compute 1D, 2D, SPF 3D,

55 and 3D flow velocities and flow displacement time series and linear rates; we also stabilize the solution using zeroth, first, and second-order Tikhonov regularization.

The SAR-derived displacements for a single epoch can be transformed into 3D (north, east, vertical) displacements by either combining multiple data sets or assuming various model constraints (Mohr et al., 1998; Wright et al., 2004; Gourmelen et al.,

2007; Kumar et al., 2011; Hu et al., 2014). However, the 3D displacement time series cannot be computed with available tech-
niques due to limitations inherent in the data acquisition strategy. For example, SAR data on ascending and descending orbits
are acquired at different days, often with different incidence angles, temporal and spatial resolutions and even wavelengths.

The technique presented here overcomes the limitations described above to compute the 3D flow displacement time series
from ascending and descending range and azimuth SAR measurements, combined together using the MSBAS method (Sam-
sonov and d'Oreye, 2012). We focus on dynamic changes along five land-terminating glaciers in southeastern Alaska during
20 October 2016 - 23 September 2020: Agassiz, Seward, Malaspina, Klutlan and Walsh Glaciers (Figure 1). The Malaspina
Glacier is the world's largest piedmont glacier covering approximately 2200 km^2 on the flat coastal foreland (Sharp, 1958;
Muskett et al., 2003; Sauber et al., 2005) and is partially fed by Seward Glacier, a surge-type glacier that originates in the
upper reaches of Mt. Logan (Sharp, 1951; Ford et al., 2003). A mass budget deficit in the Malaspina-Seward complex has long
been recognized (Sharp, 1951). Agassiz Glacier is another surge-type that flows in an adjacent sinuous valley northwest of the
Malaspina-Seward complex (Muskett et al., 2003; Sauber et al., 2005). The Klutlan Glacier is an 82-km long surge-type valley
glacier located at elevations between 1300 and 2100 m; it has surged repeatedly over the last few hundred years (Wright, 1980;
Driscoll, 1980). Walsh Glacier is a 90-km long surge-type valley glacier located at a higher elevation of about 1500-3000. It is
fed by two major branches, one from the north and one from the east and converges with the Logan Glacier downstream (Fu
and Zhou, 2020). Our results demonstrate that this new technique can be used to analyze 3D flow velocities of glacier surfaces
over large regional scales using nearly 30 years of archived SAR data and for near real-time monitoring of these glaciers us-
ing rapid revisit SAR data from satellites, such as Sentinel-1 (6 days revisit period) and forthcoming NISAR (12 days revisit
period).

2 Data and Model

We downloaded 198 ascending (track 123) and 214 descending (track 116) Sentinel-1 single-look complex (SLC) images
from the NASA Distributed Active Archive Center (DAAC) operated by the Alaska Satellite Facility (ASF) (Table 1). Two
ascending and two descending frames along the azimuth directions were concatenated for each, resulting in 99 and 107 swaths,
respectfully. Ascending and descending sets were processed individually using GAMMA software (Wegmuller and Werner,
1997) that produced range and azimuth offsets for consecutive pairs (Figure 3). To compute offsets, we used a 64×16 pixels
sampling interval and 256×256 pixels correlation window. Such a large window was required to obtain a distinct peak of the
2D cross-correlation function. Offsets were spatially filtered using a median filter with a 2 km (6 sigma) filter-width, geocoded
using TerraSAR-x 90 m DEM and resampled to a common grid with a ground resolution of 200 m.

The 3D displacement time series were computed by inverting a set of linear equations, first solving for the north, east and vertical flow velocities $V_{n,e,v}$ for each acquisition epoch and then for cumulative 3D flow displacements $D_{n,e,v}$

$$\begin{pmatrix} A \\ \lambda L \end{pmatrix} \begin{pmatrix} V_n \\ V_e \\ V_v \end{pmatrix} = \begin{pmatrix} RO_{asc} \\ AO_{asc} \\ RO_{dsc} \\ AO_{dsc} \\ 0 \end{pmatrix}, \quad D_{n,e,v}^{i+1} = D_{n,e,v}^{i} + V_{n,e,v}^{i}\Delta t^{i}. \tag{1}$$

90   Here, in a matrix form, RO are the range and AO are the azimuth offsets computed from Sentinel-1 data; L is the Tikhonov regularization matrix multiplied by the regularization parameter, λ, and A is the transform matrix constructed from the time intervals between consecutive SAR acquisitions and the range S_r and azimuth S_a directional cosines with north, east, and vertical components

$$S_r = \{S_{nr}, S_{er}, S_{vr}\} = \{\sin(\phi)\sin(\theta), -\cos(\phi)\sin(\theta), \cos(\theta)\}$$
$$S_a = \{S_{na}, S_{ea}, S_{va}\} = \{\cos(\phi), \sin(\phi), 0\}, \tag{2}$$

95   where ϕ is the azimuth and θ is the incidence angles.

The structure of the transform matrix A used in this 3D case can be deduced from a simplified example shown in Figure 2 and described below. In this example, it is assumed that ascending sets consist of three SAR images acquired on t_0, t_2, and t_4 and descending set consists of four SAR images acquired on t_{-1}, t_1, t_3, and t_5. Two ascending range ρ_{0-2}^{asc}, ρ_{2-4}^{asc} and azimuth α_{0-2}^{asc}, α_{2-4}^{asc} offsets are computed from three ascending SAR images and three descending range ρ_{-1-1}^{dsc}, ρ_{1-3}^{dsc}, ρ_{3-5}^{dsc}

100   and azimuth α_{-1-1}^{dsc}, α_{1-3}^{dsc} α_{3-5}^{dsc} offsets are computed from four descending SAR images. Boundary correction (shown as blue arrows in Figure 2) is applied to the first and last descending offsets ρ_{-1-1}^{dsc}, α_{-1-1}^{dsc}, ρ_{3-5}^{dsc}, and α_{3-5}^{dsc} by multiplying by $(t_1 - t_0)/(t_1 - t_{-1})$ and $(t_4 - t_3)/(t_5 - t_3)$ in order to adjust the coverage to match the ascending offsets. In this simplified

example, equation (1) becomes:

$$
\begin{pmatrix}
s_{nr}^{asc}\Delta t_0 & s_{er}^{asc}\Delta t_0 & s_{vr}^{asc}\Delta t_0 & s_{nr}^{asc}\Delta t_1 & s_{er}^{asc}\Delta t_1 & s_{vr}^{asc}\Delta t_1 & 0 & 0 & 0 & 0 & 0 & 0 \\
0 & 0 & 0 & 0 & 0 & 0 & s_{nr}^{asc}\Delta t_2 & s_{er}^{asc}\Delta t_2 & s_{vr}^{asc}\Delta t_2 & s_{nr}^{asc}\Delta t_3 & s_{er}^{asc}\Delta t_3 & s_{vr}^{asc}\Delta t_3 \\
s_{na}^{asc}\Delta t_0 & s_{ea}^{asc}\Delta t_0 & 0 & s_{na}^{asc}\Delta t_1 & s_{ea}^{asc}\Delta t_1 & 0 & 0 & 0 & 0 & 0 & 0 & 0 \\
0 & 0 & 0 & 0 & 0 & 0 & s_{na}^{asc}\Delta t_2 & s_{ea}^{asc}\Delta t_2 & 0 & s_{na}^{asc}\Delta t_3 & s_{ea}^{asc}\Delta t_3 & 0 \\
s_{nr}^{dsc}\Delta t_0 & s_{er}^{dsc}\Delta t_0 & s_{vr}^{dsc}\Delta t_0 & 0 & 0 & 0 & 0 & 0 & 0 & 0 & 0 & 0 \\
0 & 0 & 0 & s_{nr}^{dsc}\Delta t_1 & s_{er}^{dsc}\Delta t_1 & s_{vr}^{dsc}\Delta t_1 & s_{nr}^{dsc}\Delta t_2 & s_{er}^{dsc}\Delta t_2 & s_{vr}^{dsc}\Delta t_2 & 0 & 0 & 0 \\
0 & 0 & 0 & 0 & 0 & 0 & 0 & 0 & 0 & s_{nr}^{dsc}\Delta t_3 & s_{er}^{dsc}\Delta t_3 & s_{vr}^{dsc}\Delta t_3 \\
s_{na}^{dsc}\Delta t_0 & s_{ea}^{dsc}\Delta t_0 & 0 & 0 & 0 & 0 & 0 & 0 & 0 & 0 & 0 & 0 \\
0 & 0 & 0 & s_{na}^{dsc}\Delta t_1 & s_{ea}^{dsc}\Delta t_1 & 0 & s_{na}^{dsc}\Delta t_2 & s_{ea}^{dsc}\Delta t_2 & 0 & 0 & 0 & 0 \\
0 & 0 & 0 & 0 & 0 & 0 & 0 & 0 & 0 & s_{na}^{dsc}\Delta t_3 & s_{ea}^{dsc}\Delta t_3 & 0 \\
\lambda & 0 & 0 & -\lambda & 0 & 0 & 0 & 0 & 0 & 0 & 0 & 0 \\
0 & \lambda & 0 & 0 & -\lambda & 0 & 0 & 0 & 0 & 0 & 0 & 0 \\
0 & 0 & \lambda & 0 & 0 & -\lambda & 0 & 0 & 0 & 0 & 0 & 0 \\
0 & 0 & 0 & \lambda & 0 & 0 & -\lambda & 0 & 0 & 0 & 0 & 0 \\
0 & 0 & 0 & 0 & \lambda & 0 & 0 & -\lambda & 0 & 0 & 0 & 0 \\
0 & 0 & 0 & 0 & 0 & \lambda & 0 & 0 & -\lambda & 0 & 0 & 0 \\
0 & 0 & 0 & 0 & 0 & 0 & \lambda & 0 & 0 & -\lambda & 0 & 0 \\
0 & 0 & 0 & 0 & 0 & 0 & 0 & \lambda & 0 & 0 & -\lambda & 0 \\
0 & 0 & 0 & 0 & 0 & 0 & 0 & 0 & \lambda & 0 & 0 & -\lambda
\end{pmatrix}
\begin{pmatrix}
V_n^0 \\ V_e^0 \\ V_v^0 \\ V_n^1 \\ V_e^1 \\ V_v^1 \\ V_n^2 \\ V_e^2 \\ V_v^2 \\ V_n^3 \\ V_e^4 \\ V_v^4
\end{pmatrix}
=
\begin{pmatrix}
\rho_1^{asc} \\ \rho_2^{asc} \\ \alpha_1^{asc} \\ \alpha_2^{asc} \\ \rho_1^{dsc} \\ \rho_2^{dsc} \\ \rho_3^{dsc} \\ \alpha_1^{dsc} \\ \alpha_2^{dsc} \\ \alpha_3^{dsc} \\ 0 \\ 0 \\ 0 \\ 0 \\ 0 \\ 0 \\ 0 \\ 0 \\ 0
\end{pmatrix}.
\tag{3}
$$

105   The original MSBAS methodology, developed for DInSAR data, combines multiple data sets acquired at different times and in various observational geometries. The 2D (east and vertical) method was described in (Samsonov and d'Oreye, 2012, 2017) and the surface-parallel-flow constrained 3D (north, east, vertical) method in (Samsonov, 2019; Samsonov et al., 2020). The novel unconstrained 3D method presented here uses both range and azimuth measurements for computing 3D displacements. This work is now possible due to the improved availability over large areas of high-quality, high-resolution, temporally-dense

110   ascending and descending SAR data and the increase in computational power that allows computing a large amount of range and azimuth offset maps and inverting large matrices. Since this method does not make any assumptions about the direction of motion, it provides the optimal solution applicable to any phenomenon (e.g. glacier flow, tectonic and anthropogenic deformation, etc). The typical size of the transform matrix A exceeds 100s and often 1000s of columns and rows for each coherent pixel. It is 609×1014 in our case. The singular value decomposition (SVD) algorithm from the Linear Algebra PACKage (LA-

115   PACK) library called from C++ code is used for inverting this matrix for each coherent pixel. Depending on the number of cores in the processing unit and the number of pixels, this process can take from several hours to several days.

First-order Tikhonov regularization was applied during the inversion, resulting in temporal smoothing. The magnitude of smoothing is controlled by the regularization parameter λ that can be selected, for example, using the L-curve method (Hansen and O'Leary, 1993; Samsonov and d'Oreye, 2017). The choice of a regularization order is not critical in our case; for example,

120   the second-order Tikhonov regularization produces visually indistinguishable results.

An estimate of the 3D mean linear flow velocity was computed from cumulative flow displacements. A straight line was fit to the 3D flow displacement time series and then divided by the total length of time of the record, here three years. For aesthetic

purposes, horizontal flow velocity was resampled to a coarser resolution and values less than 5 m/year were removed. Areas of interest were reduced to three small sub-regions (AOI1, AOI2 and AOI3 in Figure 1) that cover only five glaciers.

3 Results

The SAR intensity images (Figures 4(a), 5(a) and 6(a)) show five glaciers in detail: Agassiz (AG), Malaspina (MG), Seward (SG), Klutlan (KG) and Walsh (WG) Glaciers. Mean horizontal and vertical linear flow velocities are shown in Figures 4(b), 5(b) and 6(b). Horizontal flow velocity is shown as vectors and vertical flow velocity is colour-coded, with red colour representing downward motion. The fastest horizontal flow velocities exceed 1000 m/year and the fastest vertical flow velocities exceed 200 m/year. Overall, Seward Glacier experiences the fastest motion and Malaspina Glacier experiences the slowest motion (Figure 4(b)); vertical flow is predominately downward along these two glaciers. In contrast, vertical flow velocities along the Klutlan (Figure 5(b)) and Walsh (Figure 6(b)) Glaciers changes direction a number of times.

The direction and magnitude of mean linear flow velocities sampled along profiles AB from Malaspina and Seward Glaciers, CD from Klutlan Glacier and EF from Walsh Glacier are shown in Figures 4(c), 5(c) and 6(c) as vectors with tails that start at the surface elevation of each glacier. The animations of flow velocity time series, sampled along these profiles are also provided. Note that the vertical axis (surface elevation) and horizontal axis (distance along profile) are scaled differently, producing significant angular distortion in flow velocity and topographic slopes by factors of 47, 20 and 17, respectfully. The mean linear flow velocities provide insight into the direction and magnitude of mean velocities calculated over a specific interval (e.g. the Sentinel-1 record); however, these values can vary over time. This is evident in the temporal evolution of the 3D velocity magnitudes sampled along these profiles for the Seward and Malaspina Glaciers (Fig. 4(d)), the Klutlan Glacier (Fig. 5(d)), and the Walsh Glacier (Fig. 6(d)). Flow along the lower reaches of the Malaspina Glacier seasonally varies with flow increasing during winter months and decreasing during summer; although, the seasonal acceleration in flow was delayed in 2020 and of higher magnitude. Seasonal flow along the Klutlan and Walsh Glaciers is far less pronounced; however, each shows an episodic shift in flow occurred around mid-2018 and mid-2017, respectively.

Examples of 3D flow displacement time series for 5×5 pixel regions P1-P9 are shown in Figure 7. Similar time series are available for each coloured pixel in Figures 4-6; the locations selected were chosen to demonstrate diverse ice dynamic observations possible with the MSBAS-3D method. Regions P1 and P2 are located on the lower lobes of the Malaspina Glacier, at an elevation of about 200 m above sea level. Horizontal and vertical flow velocities at these regions are only about 10 m/year, with a seasonal signal clearly evident in the vertical component. The displacement time series show that flow is predominately west-southwest at P1 and southeast at P2. An abrupt change in a flow regime occurred at P1 at the end of June 2020. Since then, the flow velocity at P1 has remained elevated in comparison to the values observed in prior years. This many-fold velocity increase can also be observed in Fig 4d along the later part of the profile AB (>35000 m). Regions P3 and P4 are located on Malaspina and Seward Glaciers at elevations of about 550 and 1000 m. At these locations, horizontal flow dominates flow displacement, while vertical flow displacement is minimal. The southwest direction of flow is persistent at both locations. A

155 small seasonal signal is observed in the north component at P3. Flow velocities along the main branch of the Agassiz Glacier, not shown, are very similar to the flow velocities along Seward glacier but of a lesser magnitude.

Regions P5-P8 are located on Klutlan Glacier at elevations of about 2100, 1650, 1450, and 1400 m, respectively. The vertical flow is downward at regions P5 and P7 and upward at a region P8. Horizontal and vertical flow velocities show significant variability in magnitude at regions P6, P7 and P8 while preserving their general flow direction.

160 Region P9 is located on Walsh glacier at an elevation of about 1900 m. Here, northwest upward displacement is observed until July 2017 when a gradual reduction occurred. Error bars throughout Figure 7 show measurement variability within the 5×5 pixel region, rather than precision, though both quantities are likely related.

4 Discussion

The technique presented in this study is a viable solution for computing 3D flow displacement time series from ascending
165 and descending range and azimuth SAR measurements. Range offsets can be substituted or complemented with DInSAR measurements since both measure the same quantity with different scales; similarly, azimuth offsets can be substituted or complemented with Multiple Aperture Interferometry (MAI) (Bechor and Zebker, 2006) measurements. For high resolution, SAR data, the precision of the SPO technique approaches that of DInSAR. In addition to glaciers, this technique can be used for studying other geophysical processes (e.g. landslides, sea/river/lake ice drift) if their motion exceeds the sensitivity of
170 SPO and/or MAI techniques. Our approach is conceptually similar to the technique of Guo et al. (2020) that was built on our previous work. However, our software can additionally compute 1D, 2D, SPF 3D and 3D flow velocities and flow displacement time series and linear rates. The solution is stabilized using zeroth, first, and second-order Tikhonov regularization (Samsonov and d'Oreye, 2017).

We compared the magnitude of mean horizontal flow velocities along the three profiles with the results presented in (Gardner
175 et al., 2019) (Figure S1). There, surface velocities are derived from Landsat 4, 5, 7, and 8 imagery over the time period from 1985 to 2018 using the auto-RIFT feature tacking processing chain described in Gardner et al. (2018). Both data sets show reasonable agreement. We observe that in areas experiencing nearly constant flow velocity (e.g. Seward and Malaspina glaciers), both datasets show nearly identical results. The SAR-derived velocities are lower in the upper part of the Seward Glacier, which is likely due to the filtering effect that naturally reduces velocity magnitude. Significant filtering is required in
180 our processing because, for time series analysis, every single range and azimuth offset maps must be coherent at every pixel, which can be only achieved by using large correlation window followed by strong filtering. At Klutlan and Walsh Glaciers, SAR-derived velocities are affected by the surges, which are not reflected in (Gardner et al., 2019) results. Overall, in addition to providing the three components of flow velocity at a high temporal resolution, our study demonstrates that deviations from the mean flow velocity can be very significant.

185 SAR-derived time series are often compared with the GNSS-derived time series and both techniques are considered conceptually similar; however, there is an important difference between the two, particularly when applied to glacier flow. SAR measures displacement within fixed geophysical locations (Eulerian representation), while GNSS measurements track receivers

that are mounted to non-stationary geophysical surfaces (Lagrangian representation). Lagrangian displacement time series describes a trajectory of an object in space as a function of time, whereas the Eulerian displacement time series describes the

190   cumulative length (of ice, rock, etc) that flows through a fixed geophysical location. While the distinction between these reference frames is well established in the glaciological community, it is less known in the solid-earth geophysical community (Samsonov and Tiampo, 2006; Samsonov et al., 2007; Gourmelen et al., 2010; Shen and Liu, 2020). For the latter, GNSS and SAR measurements can be considered nearly identical only when flow velocity at a fixed geophysical location (i.e. SAR pixel) is equal to the flow velocity at the GNSS site; that is when GNSS-derived displacements are contained within a single SAR

195   pixel. This occurs when the flow velocity is very small and the material is rigid, as in tectonic deformation studies. For rapidly deforming glacier surfaces, the differentiation is far more critical. Although the time-series in Figure 7 resemble GNSS-derived displacements, it is important to remember that these Eulerian measurements represent the cumulative displacement at any one pixel over time. Hence to emphasize this difference, we use the *flow displacement* terminology.

Flow velocity time series can be used as an alternative and perhaps more intuitive way of presenting SAR-derived Eulerian

200   measurements. For example, time series of the vertical flow velocities at region P2 are plotted in Figure 7(b) (black '+'). These results appear noisier than the flow displacement time series, which makes the interpretation more difficult; to simplify the interpretation we fitted a harmonic function (red line). Flow displacement time series can also be used to identify directional changes in ice flow. For our example, the subtle change in flow direction at P2 along the Malaspina Glacier (Figure 7b) occurred in a region of unconfined flow along the glacier's lower lobe, and thus is somewhat expected and not overly concerning.

205   However, similar changes within regions of confined flow such as outlet glaciers or ice streams could indicate a regime shift in ice dynamics (Conway et al., 2002; Siegert et al., 2004; Hulbe and Fahnestock, 2007), which can have important implications for the long-term stability of glaciers and ice sheets. Moreover, such directional changes are not as easily discerned in 2D or 3D resolved velocity fields. It is a matter of personal preference to use either flow velocity or flow displacement time series as both convey similar information; however, the flow displacement time series extracted along a profile can be used to identify

210   dominant flow components (north, east, or vertical) or for precisely identifying episodic changes in glacier flow.

The overall direction of vertical flow is down along the entire lengths of the Seward and Malaspina Glaciers (Figure 4b,c). The downward flow is expected in the upper reaches of accumulation zones because of firn compaction, and in areas with steeply dipping surfaces due to sloping bed topography; however, downward flow in the lower ablation zone is more concerning. In general, the accumulation of snow and ice in high elevations produces a net mass gain that replenishes ice lost through

215   ablation processes along the lower glacier. In steady-state, these processes balance each other and lead to submergent flow in the accumulation zone and emergent flow in the ablation zone; thus, ice mass lost through melt in the ablation zone is replenished by ice that emerges from the depths of ice columns to the glacier surface to maintain a consistent surface elevation (Hooke, 2019). The predominately downward flow of ice observed throughout the Malaspina Glacier's massive lobe (Figure 4b,c) indicates that ablation rates have exceeded emergence velocities during our 4 year study period, implying that the glacier

220   is still adjusting to climatic warming. Indeed, the Seward, Malaspina, and Agassiz Glaciers are not in a steady-state. Seasonal variability is observed along the Seward and Malaspina Glaciers (Figures 4(d), 7(b)-7(c)). The fastest motion occurs during

winter and the slowest flow in summer, consistent with other glaciers in the region (Abe et al, 2015; Vijay and Braun, 2017; Enderlin et al, 2017).

Velocities along Klutlan Glacier vary in more complex and interesting ways with multiple zones of upward and downward
225 flow observed. This surge-type glacier (RGIConsortium, 2017) has a 30 (Meier and Post, 1969) to 60-year surge cycle (Wright, 1980; Driscoll, 1980). Altena et al. (2019) used optical satellite data to show its most recent surge initiated in 2014 and continued through 2017. The surge started mid-glacier and had two propagating fronts: a dominant surge front that propagated downglacier and a secondary subdued front that propagated upglacier. Our SAR-based record shows that surge activity terminated in mid-2018. More significantly, our 3D velocity fields show the vertical component of motion from the kinematic wave
230 that propagated down the glacier. For example, P7 (Figure 7) shows surface displacements are minimal during the first half of 2017, increase slightly in summer, again in the fall, and then experience the greatest displacement during Spring 2018; vertical displacements are consistently downward throughout. In contrast, the displacement 10 km downglacier at P8 is more persistent and continues well into the 2018 summer; the vertical component here shows uplift. The timing coincides with the propagation of the surge front into the lower glacier (P8) in early 2018 (see Fig 12a in Altena et al. (2019), approximately 55 km along the
235 profile). Thus, the downward vertical motion at P7 and upward motion at P8 represents the kinematic wave of the surge front advecting down the glacier between these two points, data that cannot be extracted from optical or traditional 2D SAR data processing.

The Walsh Glacier is another surge-type glacier with recent surge activity. Using optical Landsat data, Fu and Zhou (2020) showed the latest surge initiated prior to 2015. Our SAR-based observations show residual surge activity continued into 2017
240 and abruptly ended in mid-2017 (Figure 6(d)). It is of notice that while horizontal components are consistent across the glacier valley, the vertical component shows areas of upward and downward flow (Figures 5(b) and 6(b)). Such a complex flow pattern can only be derived from side-looking SAR measurements that capture horizontal and vertical components of motion.

SAR measures glacier motion at a certain depth rather than at the surface. Previous studies for this region suggest that the C-band SAR penetrates about four meters into the glacier's firn layer in dry conditions (Rignot et al., 2001). The penetration
245 depth is affected by water content and thus varies by season; it is likely that some fraction of the signals observed in Figures 4-7 is due to the seasonal fluctuation in the penetration depth. A combination of SAR and optical data in a complementary manner could provide useful information about the variation of flow velocity with depth throughout different seasons.

5 Conclusions

We presented a novel flow displacement technique to observe variations in glacier surface flow in 3D using ascending and
250 descending SAR scenes. The 3D flow displacement (and/or velocity) time series computed allowed us to map in unprecedented detail the state and the temporal evolution of five glaciers in Southeast Alaska during 20 October 2016 - 23 September 2020. On a broader scale, this technique can be used for reconstructing the historic response of the worldwide glaciers to the warming climate using over 30 years of available satellite SAR records. The horizontal components can be resolved to study flow variations over time, and if integrated along a profile that is perpendicular to flow, ice flux. The vertical component can be used

to assess changes in vertical ice flux or changes in surface slope over time, which is useful for studying glacier surge dynamics or variations in driving stress as a glacier dynamically adjusts to a changing climate. The software is freely available to the research community.

Video supplement. The animations of flow velocity time series, sampled along profiles AB, CD and EF are provided (files seward.gif, klutlan.gif and walsh.gif).

Author contributions. Sergey Samsonov - Conceptualization; Data curation; Formal analysis; Investigation; Methodology; Project administration; Resources; Software; Visualization; Writing - original draft; Writing - review & editing. Kristy Tiampo - Investigation; Formal analysis; Methodology; Writing - review & editing. Ryan Cassotto - Investigation; Formal analysis; Methodology; Writing - review & editing.

Competing interests. No competing interests are present.

Acknowledgements. We thank the European Space Agency for acquiring and the National Aeronautics and Space Administration (NASA) and ASF for distributing Sentinel-1 SAR data. Figures were plotted with GMT and Gnuplot software. Work of Sergey Samsonov was supported by the Canadian Space Agency through the Data Utilization and Application Plan (DUAP) program. The work of Kristy Tiampo was supported by CIRES, University of Colorado Boulder. The work of Ryan Cassotto was supported by NASA Grant No. 80NSSC17K0017.

References

270 Altena, B., Scambos, T., Fahnestock, M., and Kääb, A.: Extracting recent short-term glacier velocity evolution over southern Alaska and the Yukon from a large collection of Landsat data, The Cryosphere, 13, 795–814, https://doi.org/10.5194/tc-13-795-2019, 2019.

Arendt, A.: Assessing the Status of Alaska's Glaciers, Science, 332, 1044–1045, https://doi.org/10.1126/science.1204400, 2011.

Arendt, A., Walsh, J., and Harrison, W.: Changes of glaciers and climate in northwestern North America during the late twentieth century, Journal of Climate, 22, 4117–4134, https://doi.org/10.1175/2009JCLI2784.1, 2009.

275 Bartholomew, I., Nienow, P., Mair, D., Hubbard, A., King, M., and Sole, A.: Seasonal evolution of subglacial drainage and acceleration in a Greenland outlet glacier., Nature Geoscience, 3, 408–411, https://doi.org/10.1038/ngeo863, 2010.

Bechor, N. and Zebker, H.: Measuring two-dimensional movements using a single InSAR pair, Geophysical Research Letters, 33, https://doi.org/10.1029/2006GL026883, 2006.

Berthier, E., Vadon, H., Baratoux, D., Arnaud, Y., Vincent, C., Feigl, K., Remy, F., and Legresy, B.: Surface motion of mountain glaciers
280 derived from satellite optical imagery, Remote Sensing of Environment, 95, 14 – 28, https://doi.org/10.1016/j.rse.2004.11.005, 2005.

Bisset, R., Dehecq, A., Goldberg, D., Huss, M., Bingham, R., and Gourmelen, N.: Reversed Surface-Mass-Balance Gradients on Himalayan Debris-Covered Glaciers Inferred from Remote Sensing., Remote Sensing, 12, 1563, https://doi.org/10.3390/rs12101563, 2020.

Burgess, E., Forster, R., and Larsen, C.: Flow velocities of Alaskan glaciers, Nature Communications, 4, https://doi.org/10.1038/ncomms3146, 2013.

285 Conway, H., Catania, G., Raymond, C., Gades, A., Scambos, T., and Engelhardt, H.: Switch of flow direction in an Antarctic ice stream, Nature, 419, 465–467, https://doi.org/10.1038/nature0108, 2002.

Dehecq, A., Gourmelen, N., and Trouve, E.: Deriving large-scale glacier velocities from a complete satellite archive: Application to the Pamir–Karakoram–Himalaya, Remote Sensing of Environment, 162, 55 – 66, https://doi.org/10.1016/j.rse.2015.01.031, 2015.

Driscoll, F. J.: Formation of the neoglacial surge moraines of the Klutlan glacier, Yukon Territory, Canada., Quaternary Research, pp. 19–30,
290 https://doi.org/10.1016/0033-5894(80)90004-6, 1980.

Fahnestock, M., Scambos, T., Moon, T., Gardner, A., Haran, T., and Klinger, M.: Rapid large-area mapping of ice flow using Landsat 8, Remote Sensing of Environment, Remote Sensing of Environment, 185, 84–94, https://doi.org/10.1016/j.rse.2015.11.023, 2015.

Fahnestock, M., Scambos, T., Moon, T., Gardner, A., Haran, T., and Klinger, M.: Rapid large-area mapping of ice flow using Landsat 8, Remote Sensing of Environment, 185, 84–94, https://doi.org/10.1016/j.rse.2015.11.023, 2016.

295 Ford, A. L., Forster, R. R., and Bruhn, R. L.: Ice surface velocity patterns on Seward Glacier, Alaska/Yukon, and their implications for regional tectonics in the Saint Elias Mountains, Annals of Glaciology, 36, 21–28, https://doi.org/10.3189/172756403781816086, 2003.

Fu, X. and Zhou, J.: Recent surge behavior of Walsh glacier revealed by remote sensing data, Sensors, 20, 716, https://doi.org/10.3390/s20030716, 2020.

Gardner, A., Moholdt, G., Scambos, T., Fahnstock, M., Ligtenberg, S., van den Broeke, M., and Nilsson, J.: Increased West Antarctic and
300 unchanged East Antarctic ice discharge over the last 7 years, The Cryosphere, 12, 521–54, https://doi.org/10.5194/tc-12-521-2018, 2018.

Gardner, A., Fahnestock, M., and Scambos, T.: ITS_LIVE Regional Glacier and Ice Sheet Surface Velocities. Data archived at National Snow and Ice Data Center, https://doi.org/10.5067/6II6VW8LLWJ7, 2019.

Goldstein, R. M., Engelhardt, H., Kamb, B., and Frolich, R. M.: Satellite Radar Interferometry for Monitoring Ice Sheet Motion: Application to an Antarctic Ice Stream, Science, 262, 1525–1530, https://doi.org/10.1126/science.262.5139.1525, 1993.

305 Gourmelen, N., Amelung, F., Casu, F., Manzo, M., and Lanari, R.: Mining-related ground deformation in Crescent Valley, Nevada: Implications for sparse GPS networks, Geophysical Research Letters, 34, https://doi.org/10.1029/2007GL029427, 2007.

Gourmelen, N., Amelung, F., and Lanari, R.: Interferometric synthetic aperture radar–GPS integration: Interseismic strain accumulation across the Hunter Mountain fault in the eastern California shear zone, Journal of Geophysical Research: Solid Earth, 115, https://doi.org/10.1029/2009JB007064, 2010.

310 Gourmelen, N., Kim, S., Shepherd, A., Park, J., Sundal, A., Björnsson, H., and Pálsson, F.: Ice velocity determined using conventional and multiple-aperture InSAR, Earth and Planetary Science Letters, 307, 156–160, https://doi.org/10.1016/j.epsl.2011.04.026, 2011.

Gray, L.: Using multiple RADARSAT InSAR pairs to estimate a full three-dimensional solution for glacial ice movement., Geophysical Research Letters, 38, https://doi.org/1029/2010GL046484, 2011.

Gray, L., Joughin, I., Tulaczyk, S., Spikes, V., Bindschadler, R., and Jezek, K.: Evidence for subglacial water transport
315 in the West Antarctic Ice Sheet through three-dimensional satellite radar interferometry, Geophysical Research Letters, 32, https://doi.org/10.1029/2004GL021387, 2005.

Guo, L., Li, J., Li, Z.-w., Wu, L.-x., Li, X., Hu, J., Li, H.-l., Li, H.-y., Miao, Z.-l., and Li, Z.-q.: The Surge of the Hispar Glacier, Central Karakoram: SAR 3-D Flow Velocity Time Series and Thickness Changes, Journal of Geophysical Research: Solid Earth, 125, https://doi.org/10.1029/2019JB018945, 2020.

320 Hansen, P. and O'Leary, D.: The use of the L-curve in the regularization of discrete ill-posed problems, SIAM Journal on Scientific Computing, 14, 1487–1503, 1993.

Herman, F., Anderson, B., and Leprince, S.: Mountain glacier velocity variation during a retreat/advance cycle quantified using sub-pixel analysis of ASTER images, Journal of Glaciology, 57, 197–207, https://doi.org/10.3189/002214311796405942, 2011.

Hooke, R. L.: Principles of Glacier Mechanics, Cambridge University Press, 3 edn., https://doi.org/10.1017/9781108698207, 2019.

325 Hu, J., Li, Z., Ding, X., Zhu, J., Zhang, L., and Sun, Q.: Resolving three-dimensional surface displacements from InSAR measurements: A review, Earth-Science Reviews, 133, 1 – 17, https://doi.org/10.1016/j.earscirev.2014.02.005, 2014.

Hulbe, C. and Fahnestock, M.: Century-scale discharge stagnation and reactivation of the Ross ice streams, West Antarctica, Journal of Geophysical Research: Earth Surface, 112, https://doi.org/10.1029/2006JF000603, 2007.

Immerzeel, W., Kraaijenbrink, P., Shea, J., Shrestha, A., Pellicciotti, F., Bierkens, M., and de Jong, S.: High-resolution mon-
330 itoring of Himalayan glacier dynamics using unmanned aerial vehicles, Remote Sensing of Environment, 150, 93 – 103, https://doi.org/10.1016/j.rse.2014.04.025, 2014.

Joughin, I.: Ice-sheet velocity mapping: A combined interferometric and speckle-tracking approach., Annals of Glaciology, 34, 195–201, https://doi.org/10.3189/1727564027818179, 2002.

Joughin, I., Winebrenner, D., and Fahnestock, M.: Observations of ice-sheet motion in Greenland using satellite radar interferometry, Geo-
335 physical Research Letters, 22, 571–574, https://doi.org/10.1029/95GL00264, 1995.

Joughin, I., Kwok, R., and Fahnestock, M.: Interferometric estimation of three-dimensional ice-flow using ascending and descending passes., IEEE Transactions on Geoscience and Remote Sensing, 36, 25–37, https://doi.org/10.1109/36.655315, 1998.

Kumar, V., Venkataramana, G., and Høgda, K.: Glacier surface velocity estimation using SAR interferometry technique applying ascending and descending passes in Himalayas, International Journal of Applied Earth Observation and Geoinformation, 13, 545–551,
340 https://doi.org/10.1016/j.jag.2011.02.004, 2011.

Larsen, C., Burgess, E., Arendt, A. A., O'Neel, S., Johnson, A. J., and Kienholz, C.: Surface melt dominates Alaska glacier mass balance, Geophysical Research Letters, 42, 5902–5908, https://doi.org/10.1002/2015GL064349, 2015.

Massonnet, D. and Feigl, K.: Discrimination of geophysical phenomena in satellite radar interferograms, Geophysical Research Letters, 22, 1995.

345 Meier, M. and Post, A.: What are glacier surges?, Canadian Journal of Earth Sciences, 6, 807–817, https://doi.org/10.1139/e69-081, 1969.

Minchew, B. M., Simons, M., Riel, B., and Milillo, P.: Tidally induced variations in vertical and horizontal motion on Rutford Ice Stream, West Antarctica, inferred from remotely sensed observations, Journal of Geophysical Research: Earth Surface, 122, 167–190, https://doi.org/10.1002/2016JF003971, 2017.

Mohr, J., Reeh, N., and Madsen, S.: Three-dimensional glacial flow and surface elevation measured with radar interferometry., Nature, 391, 350 273–276, https://doi.org/10.1038/34635, 1998.

Morlighem, M., Rignot, E., Seroussi, H., Larour, E., Ben Dhia, H., and Aubry, D.: A mass conservation approach for mapping glacier ice thickness, Geophysical Research Letters, 38, https://doi.org/10.1029/2011GL048659, 2011.

Muskett, R. R., Lingle, C. S., Tangborn, W. V., and Rabus, B. T.: Multi-decadal elevation changes on Bagley Ice Valley and Malaspina Glacier, Alaska, Geophysical Research Letters, 30, https://doi.org/10.1029/2003GL017707, 2003.

355 Palmer, S. J., Shepherd, A., Sundal, A., Rinne, E., and Nienow, P.: InSAR observations of ice elevation and velocity fluctuations at the Flade Isblink ice cap, eastern North Greenland, Journal of Geophysical Research: Earth Surface, 115, https://doi.org/10.1029/2010JF001686, 2010.

RGIConsortium: Randolph Glacier Inventory - A Dataset of Global Glacier Outlines: Version 6.0: Technical Report, Global Land Ice Measurements from Space, Tech. rep., Colorado, USA. Digital Media., https://doi.org/10.7265/N5-RGI-60, 2017.

360 Rignot, E.: Fast Recession of a West Antarctic Glacier, Science, 281, 549–551, https://doi.org/10.1126/science.281.5376.549, 1998.

Rignot, E.: Mass balance of East Antarctic glaciers and ice shelves from satellite data., Annals of Glaciology, 34, 217–227, https://doi.org/10.3189/172756402781817419, 2002.

Rignot, E., Echelmeyer, K., and Krabill, W.: Penetration depth of interferometric synthetic-aperture radar signals in snow and ice, Geophysical Research Letters, 28, 3501–3504, https://doi.org/10.1029/2000GL012484, 2001.

365 Rignot, E., Mouginot, J., and Scheuchl, B.: Ice Flow of the Antarctic Ice Sheet, Science, 333, 1427–1430, https://doi.org/10.1126/science.1208336, http://science.sciencemag.org/content/333/6048/1427, 2011.

Rosen, P., Hensley, P., Joughin, I., Li, F., Madsen, S., Rodriguez, E., and Goldstein, R.: Synthetic aperture radar interferometry, Proceedings of the IEEE, 88, 333–382, 2000.

Samsonov, S.: Three-dimensional deformation time series of glacier motion from multiple-aperture DInSAR observation., Journal of 370 Geodesy, 93, 2651–2660, https://doi.org/10.1007/s00190-019-01325-y, 2019.

Samsonov, S. and d'Oreye, N.: Multidimensional time series analysis of ground deformation from multiple InSAR data sets applied to Virunga Volcanic Province, Geophysical Journal International, 191, 1095–1108, https://doi.org/10.1111/j.1365-246X.2012.05669.x, 2012.

Samsonov, S. and d'Oreye, N.: Multidimensional Small Baseline Subset (MSBAS) for Two-Dimensional Deformation Analysis: Case Study Mexico City, Canadian Journal of Remote Sensing, 43, https://doi.org/10.1080/07038992.2017.1344926, 2017.

375 Samsonov, S. and Tiampo, K.: Analytical optimization of DInSAR and GPS dataset for derivation of three-dimensional surface motion, Geoscience and remote sensing letters, 3, 107–111, 2006.

Samsonov, S., Tiampo, K., Rundle, J., and Li, Z.: Application of DInSAR-GPS optimization for derivation of fine scale surface motion maps of southern California, IEEE Transactions on Geoscience and Remote Sensing, 45, 512–521, 2007.

Samsonov, S., Dille, A., Dewitte, O., Kervyn, F., and d'Oreye, N.: Satellite interferometry for mapping surface deformation time series in one, two and three dimensions: A new method illustrated on a slow-moving landslide., Engineering Geology, 266, 105 471, https://doi.org/10.1016/j.enggeo.2019.105471, 2020.

Sauber, J., Molnia, B., Carabajal, C., Luthcke, S., and Muskett, R.: Ice elevations and surface change on the Malaspina Glacier, Alaska, Geophysical Research Letters, 32, https://doi.org/10.1029/2005GL023943, 2005.

Sharp, R. P.: Accumulation and ablation on the Seward-Malaspina glacier system, Canada-Alaska, GSA Bulletin, 62, 725–744, https://doi.org/10.1130/0016-7606(1951)62[725:AAAOTS]2.0.CO;2, 1951.

Sharp, R. P.: Malaspina Glacier, Alaska, Geological Society of America Bulletin, 69, 617–646, https://doi.org/10.1130/0016-7606(1958)69[617:MGA]2.0.CO;2, 1958.

Shen, Z.-K. and Liu, Z.: Integration of GPS and InSAR data for resolving 3-dimensional crustal deformation, Earth and Space Science, 7, https://doi.org/10.1029/2019EA001036, 2020.

Shepherd, A., Wingham, D. J., Mansley, J. A. D., and Corr, H. F. J.: Inland Thinning of Pine Island Glacier, West Antarctica, Science, 291, 862–864, https://doi.org/10.1126/science.291.5505.862, 2001.

Shepherd, A., Ivins, E., and Rignot, E. e. a.: Mass balance of the Greenland Ice Sheet from 1992 to 2018., Nature, 579, 233–239, https://doi.org/10.1038/s41586-019-1855-2, 2020.

Siegert, M. J., Welch, B., Morse, D., Vieli, A., Blankenship, D. D., Joughin, I., King, E. C., Vieli, G. J.-M. C. L., Payne, A. J., and Jacobel, R.: Ice Flow Direction Change in Interior West Antarctica, Science, 305, 1948–1951, https://doi.org/10.1126/science.1101072, 2004.

Strozzi, T., Luckman, A., Murray, T., and Wegmuller, U.and Werner, C. L.: Glacier motion estimation using SAR offset-tracking procedures, IEEE Transactions on Geoscience and Remote Sensing, 40, 2384–2391, https://doi.org/10.1109/TGRS.2002.805079, 2002.

van de Wal, R. S. W., Boot, W., van den Broeke, M. R., Smeets, C. J. P. P., Reijmer, C. H., Donker, J. J. A., and Oerlemans, J.: Large and Rapid Melt-Induced Velocity Changes in the Ablation Zone of the Greenland Ice Sheet, Science, 321, 111–113, https://doi.org/10.1126/science.1158540, 2008.

Waechter, A., Copland, L., and Herdes, E.: Modern glacier velocities across the Icefield Ranges, St Elias Mountains, and variability at selected glaciers from 1959 to 2012, Journal of Glaciology, 61, 624–634, https://doi.org/10.3189/2015JoG14J147, 2015.

Wang, Q., Fan, J., Zhou, W., Tong, L., Guo, Z., Liu, G., Yuan, W., Sousa, J. J., and Perski, Z.: 3D Surface velocity retrieval of mountain glacier using an offset tracking technique applied to ascending and descending SAR constellation data: a case study of the Yiga Glacier, International Journal of Digital Earth, 12, 614–624, https://doi.org/10.1080/17538947.2018.1470690, 2019.

Wegmuller, U. and Werner, C.: GAMMA SAR processor and interferometry software, in: The 3rd ERS symposium on space at the service of our environment, Florence, Italy, 1997.

Werder, M., Huss, M., Paul, F., Dehecq, A., and Farinotti, D.: A Bayesian ice thickness estimation model for large-scale applications, Journal of Glaciology, 66, 137–152, https://doi.org/10.1017/jog.2019.93, 2020.

Wright, H.: Surge Moraines of the Klutlan Glacier, Yukon Territory, Canada: Origin, Wastage, Vegetation Succession, Lake Development, and Application to the Late-Glacial of Minnesota, Quaternary Research, 14, 2–18, https://doi.org/10.1016/0033-5894(80)90003-4, 1980.

Wright, T., Parsons, B., and Lu, Z.: Toward mapping surface deformation in three dimensions using InSAR., Geophysical Research Letters, 31, 2004.

Table 1. Sentinel-1 SAR data used in this study, where θ is incidence and ϕ is azimuth angles.

	Span	$\theta°$	$\phi°$	SLC swaths
Sentinel-1 track 123 (asc)	20160816-20200930	39	342	99
Sentinel-1 track 116 (dsc)	20161020-20200923	39	198	107
Total	20161020-20200923			206
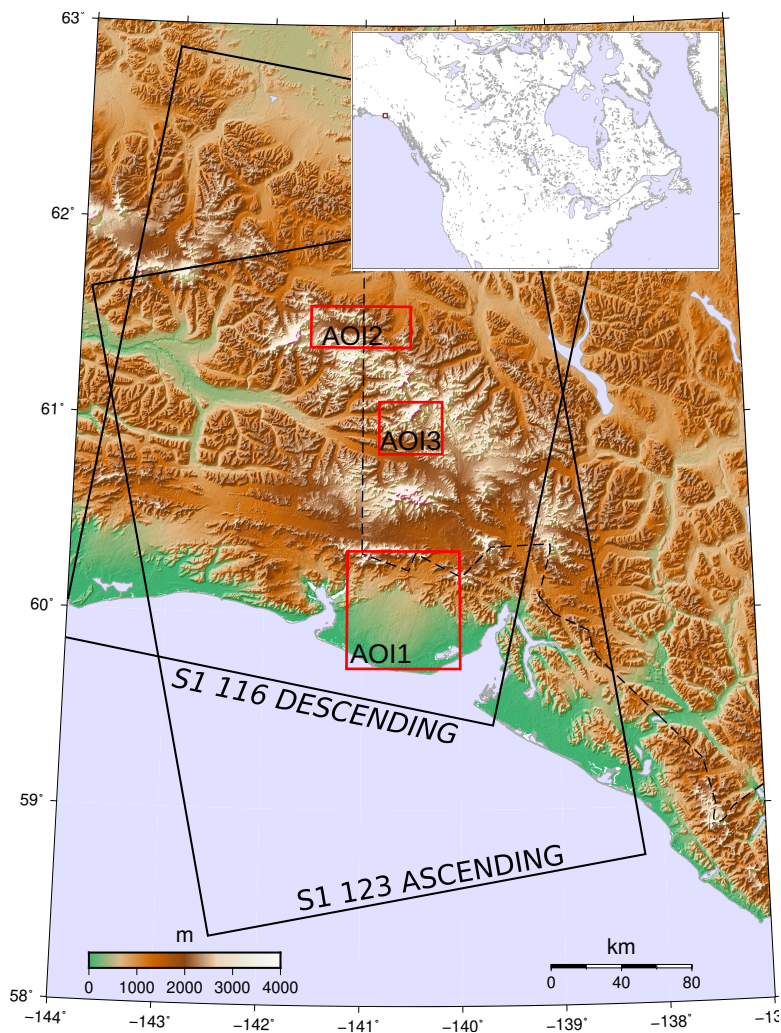
Figure 1. Outlines of three areas of interest (AOIs) in southeastern Alaska are shown in red. AOI1 covers Agassiz (AG), Malaspina (MG) and Seward (SG) Glaciers. AOI2 covers Klutlan Glacier (KG). AOI3 covers Walsh Glacier (WG). Outlines of ascending (track 123) and descending (track 116) Sentinel-1 swaths are shown in black. Background is 30 m Advanced Spaceborne Thermal Emission and Reflection Radiometer (ASTER) digital elevation model. Canada-USA border is shown as dashed black line.
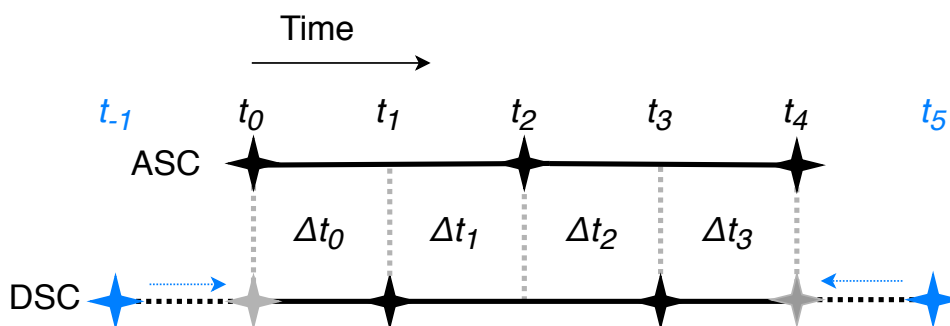
Figure 2. Schematics of simplified case described by (3). Ascending and descending SAR acquisitions at time t_i are marked with black stars. Horizontal solid lines between two octagons represent range and azimuth offset maps. Vertical dashed lines divide temporal scale in time intervals Δt_i between consecutive acquisitions. Time of first and last descending acquisitions (marked with blue stars) are adjusted to match first and last time of ascending acquisitions (marked with gray stars).
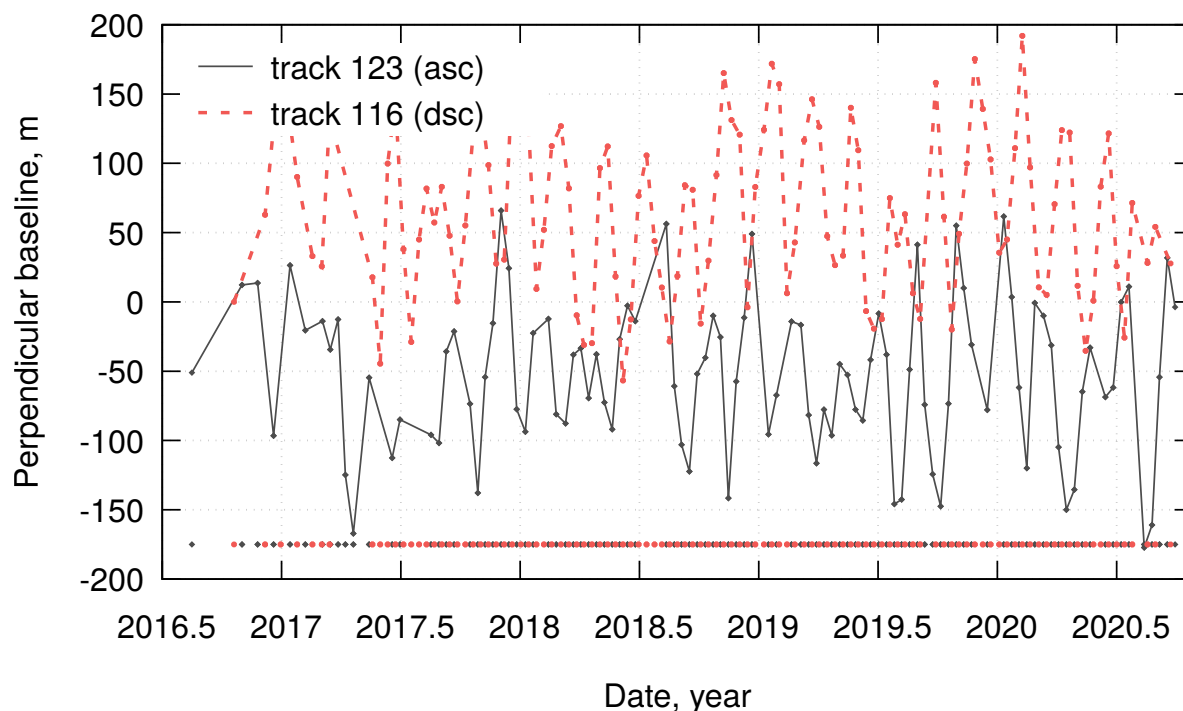
Figure 3. Spatial and temporal baselines of Sentinel-1 pairs used in this study. Mean temporal resolution is 4 days.
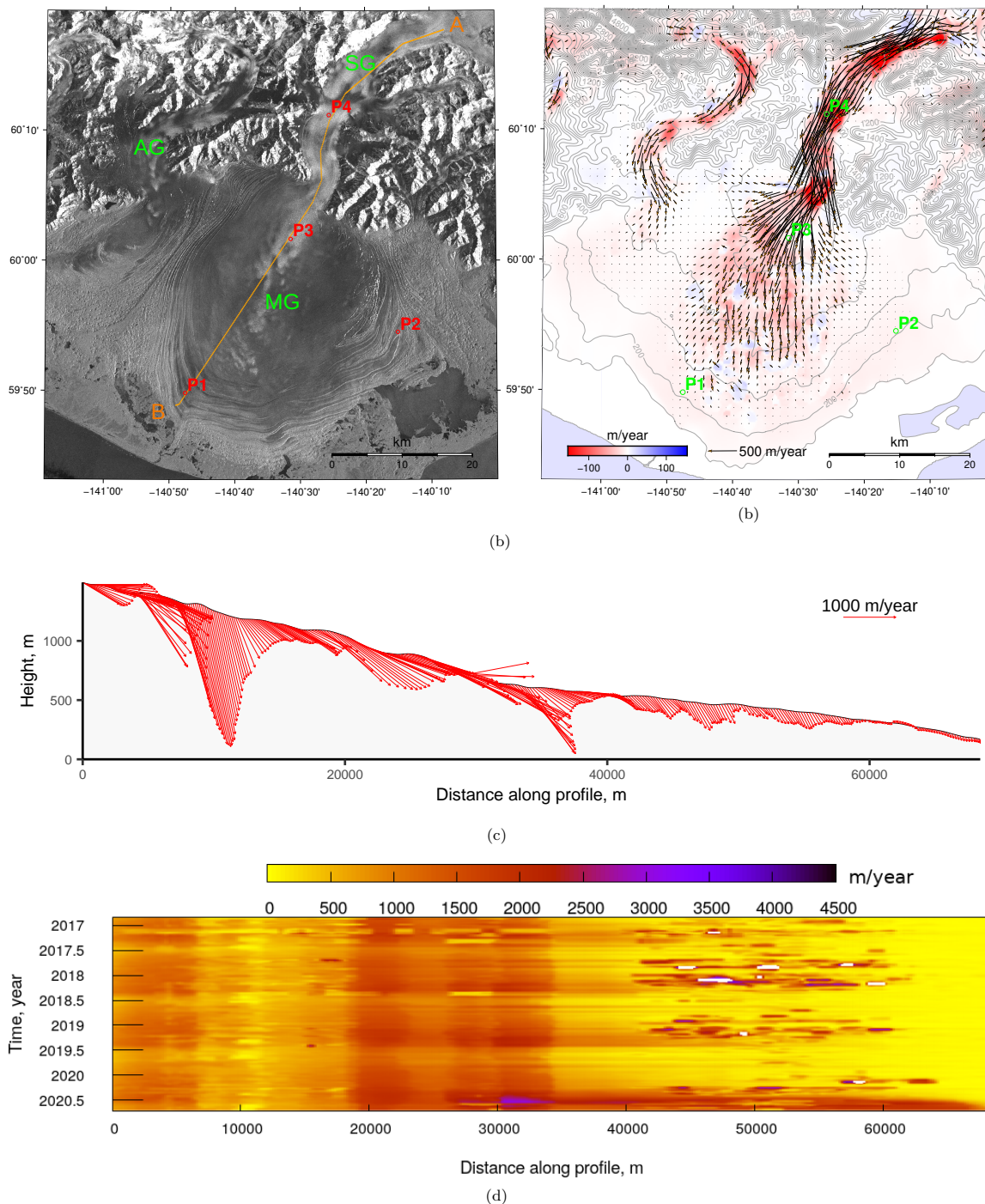
Figure 4. (a) Sentinel-1 SAR intensity image acquired on 20191222 (in YYYYMMDD format) over AOI1 that covers Agassiz, Malaspina and Seward Glaciers. (b) 3D flow velocity: horizontal velocity is shown as (coarse-resolution) vector map and vertical velocity is colour-coded. Surface topographic contour lines with intervals of 100 m are shown in grey. (c) 3D flow velocity and glacier height along profile AB, vertical axis and flow velocity slope are exaggerated by factor of 47. Flow displacement time series for regions P1-P4 are plotted in Figure 7. (d) Temporal evolution of 3D flow velocity magnitude along profile AB.
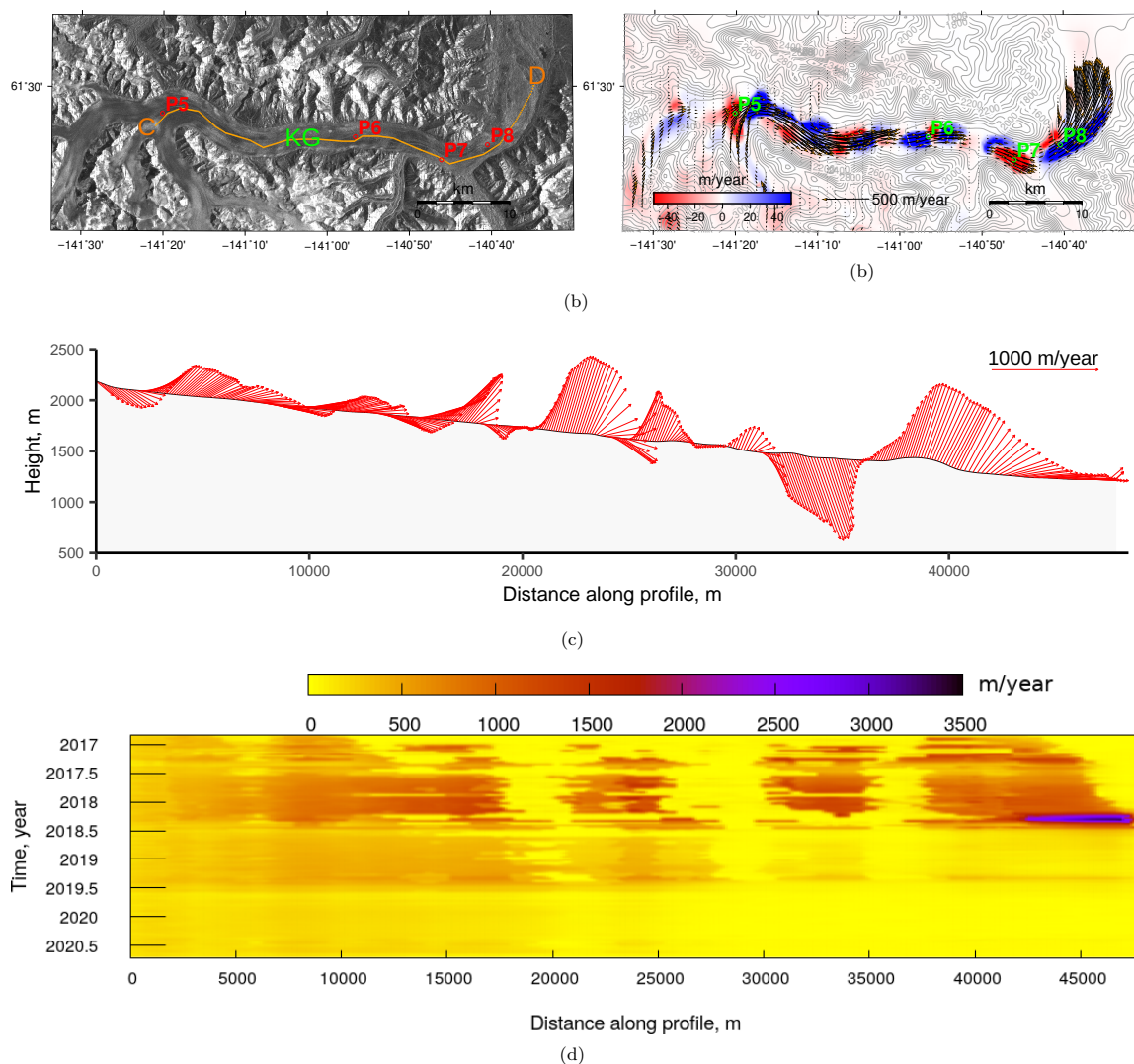
Figure 5. (a) Sentinel-1 SAR intensity image acquired on 20191222 (in YYYYMMDD format) over AOI2 that covers Klutlan Glacier. (b) 3D flow velocity: horizontal velocity is shown as (coarse-resolution) vector map and vertical velocity is colour-coded. Surface topographic contour lines with intervals of 100 m are shown in grey. (c) 3D flow velocity and glacier height along profile CD, vertical axis and flow velocity slope are exaggerated by factor of 20. Flow displacement time series for regions P5-P8 are plotted in Figure 7. (d) Temporal evolution of 3D flow velocity magnitude along profile CD.
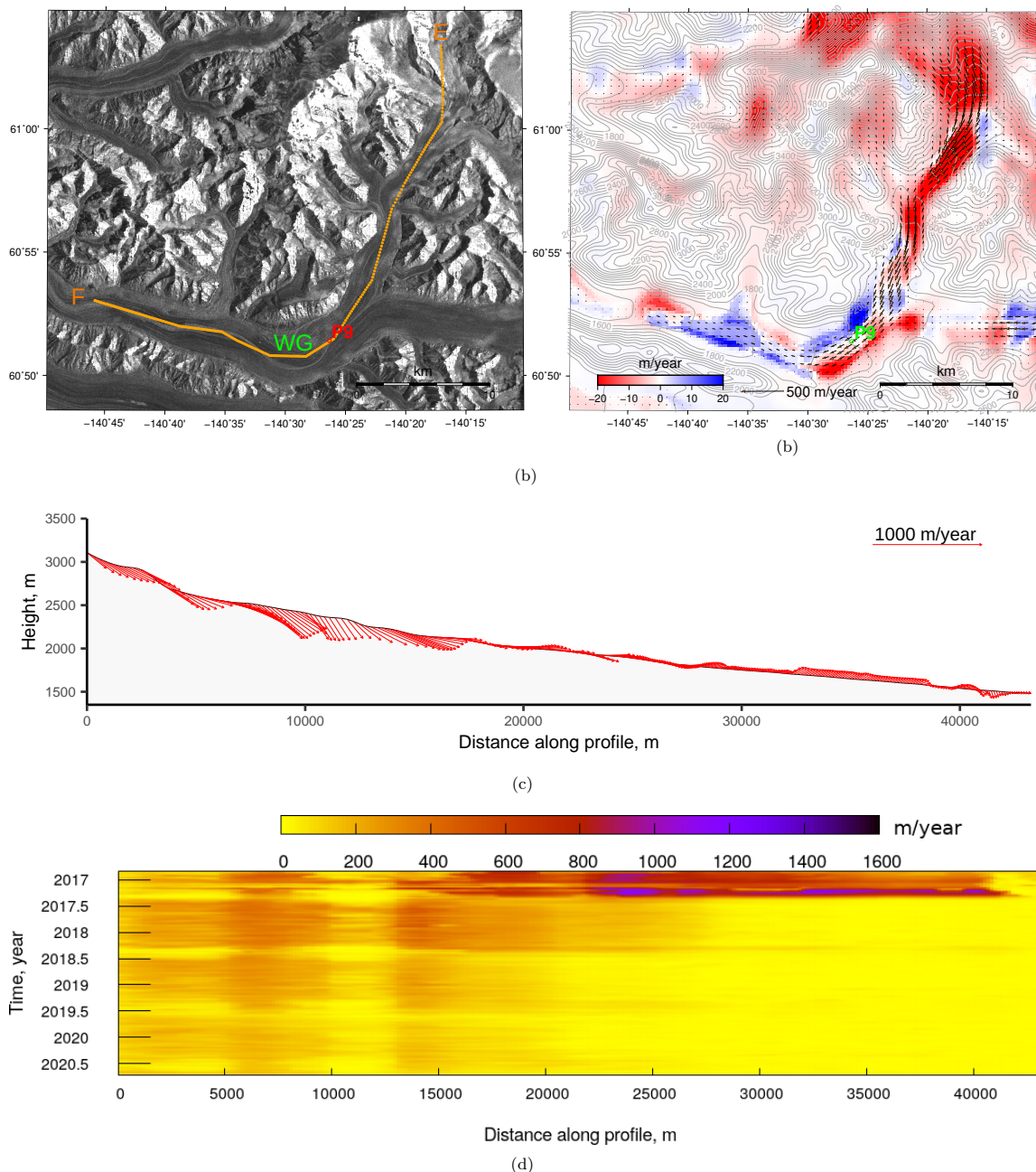
Figure 6. (a) Sentinel-1 SAR intensity image acquired on 20191222 (in YYYYMMDD format) over AOI3 that covers Walsh Glacier. (b) 3D flow velocity: horizontal velocity is shown as (coarse-resolution) vector map and vertical velocity is colour-coded. Surface topographic contour lines with intervals of 100 m are shown in grey. (c) 3D flow velocity and glacier height along profile EF, vertical axis and flow velocity slope are exaggerated by factor of 17. Flow displacement time series for region P9 is plotted in Figure 7. (d) Temporal evolution of 3D flow velocity magnitude along profile EF.
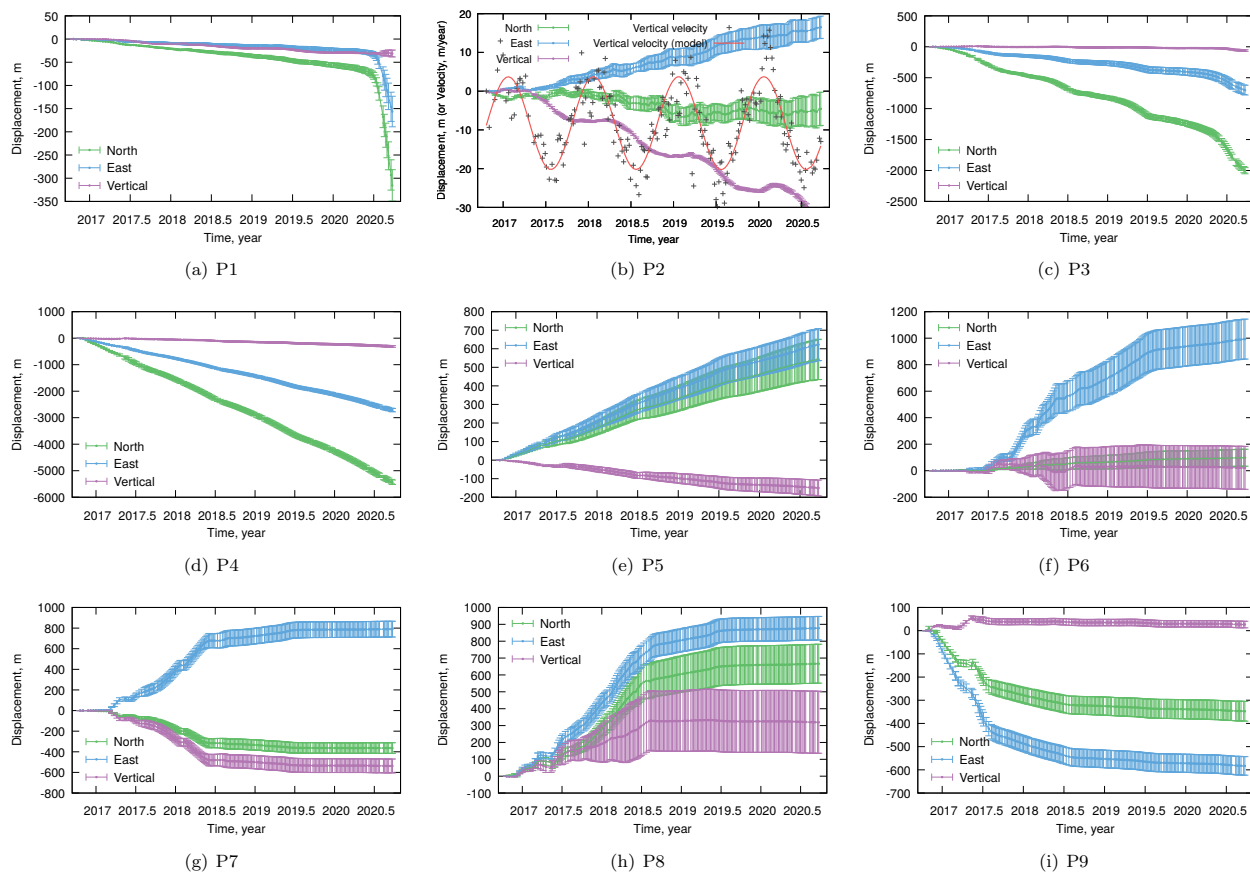
Figure 7. 3D flow displacement time series for regions P1-P9, which location is shown in Figures 4-6. For region P2 vertical flow velocity time series were also computed along with harmonic function fitted to these time series.